International Journal of Microwave and Wireless Technologies

cambridge.org/mrf

Wideband and high-directive reflective metasurface-based Fabry–Pérot cavity antennas

Mohamed F. El-Sewedy and Mahmoud Abdalla

Electronic Engineering Department, Military Technical College, Cairo, Egypt

Research Paper

Cite this article: El-Sewedy MF, Abdalla M (2023). Wideband and high-directive reflective metasurface-based Fabry–Pérot cavity antennas. *International Journal of Microwave and Wireless Technologies* **15**, 1048–1057. https://doi.org/10.1017/S1759078722001015

Received: 25 November 2021
Revised: 30 August 2022
Accepted: 1 September 2022

Key words:
5G; directivity enhancement; Fabry–Pérot cavity (FPC); high-gain antennas; highly reflective metasurface

Author for correspondence:
Mohamed F. El-Sewedy,
E-mail: mohamed.elsewedy@ieee.org

Abstract

In this work, the use of a configuration of a reflective metasurface (MS) layer is employed to design a highly directive wideband Fabry–Pérot cavity (FPC) antenna. With the use of only one MS layer and along with the achieved high directivity, the antenna's wide bandwidth, and antenna low size/cavity thickness profile are all optimized so that they are still competitive which is the main contribution of our work. The highly reflective MS layer is placed as a superstrate of a low-cost FR4 microstrip patch antenna, as the primary radiator, at a height of half-wavelength cavity condition. Thanks to the employed MS layer, most of the power is transmitted and a very small reflected power to the primary patch. The antenna is designed to serve the 28 GHz band of 5G wireless applications. At 28 GHz, the FPC antenna has a good directivity performance, with a peak simulated directive gain of 15.46 dB and measured directive gain is 14.3 dB which is a 9 dB enhancement in directivity compared to a conventional microstrip patch antenna. The antenna has a wide impedance bandwidth of 2.9 GHz which is almost three times the microstrip patch antenna bandwidth. The achieved results are for the same size of FPC antenna whose height is almost half wavelength and its overall size $2.33\lambda \times 2.33\lambda$.

Introduction

Highly directional antennas have sparked a lot of attention in recent years, particularly in millimeter-wave applications such as satellite communication and mobile systems. There are a lot of high-directive antennas such as lens antennas, parabolic reflector antennas, reflectarray antennas, and planar array antennas. Also, Fabry–Pérot cavity (FPC) antennas have a high directivity and high gain with the merits of being easier in fabrication, simpler in construction, easier in integration with the system, and more inexpensive than other above-mentioned kinds of high-gain antennas. The main emitting source, a background perfect electric conductor (PEC) layer, and a partially reflecting surface (PRS) construct an FPC antenna [1, 2]. A dipole antenna is used as a feeding source in the FPC antenna to achieve high directivity as in [2].

Researchers have focused on two major goals for developing FPC antennas. The first goal is to use an artificial magnetic conductor to reduce the profile by making the reflections have a phase shift of zero degrees and hence the profile is reduced to half compared with conventional FPC antenna with ground plane [3, 4]. The second goal is antenna gain enhancement. In [5], the use of metamaterial-inspired structures is employed to present a high directive using a holey superstrate above of microstrip patch antenna to get in-phase radiation properties and enhance the gain by 2.3 dB at 5.8 GHz. In [6], high-gain FPC antennas using metamaterial inspired superstrate is presented in which three-dimensional (3D)-metamaterial layers' superstrates with low refractive index were used to obtain a high gain at 10 GHz with a gain of 7.8 dB. Since frequency selective surface (FSS) has a pass-band behavior so it can be used as a screen forming the superstrate over a simple microstrip patch antenna. In [7], FSS characteristics of uniplanar electromagnetic (EM) bandgap were exploited to construct an FPC antenna with high gain to enhance the directivity of 6.95 dB in the broadside direction. Multilayers of FSS were used for gain enhancement [8]. But there is a problem with the large profile of FPC antennas which may restrict their applications. In [9], a zero-index metamaterial unit cell was developed to achieve a gain enhancement of 6.2 dB at 5.2 GHz by using a single-layer superstrate. Also, there are other applications of using PRS in FPC antennas as introducing dual-bands [10], wideband [11, 12], circular polarization [13, 14], gain enhancement [15], and electronic scanning [16, 17]. In [16], the authors introduced a one-dimensional leaky-wave FPC antenna to achieve electronic scanning. The antenna is built around a parallel-plate waveguide with a partially reflecting planar surface and a high impedance surface (patches with diodes) that may be adjusted to make the cavity frequency resonance conditions can be electronically tuned. The frequency band of the leaky-wave FPC antenna is at 5.6 GHz

and an electronic beam scanning range of 9–30° was achieved using the reconfigurable leaky-wave antenna. Also, a novel concept for achieving a high-gain FPC antenna was presented in [18]. A printed antenna illuminates a plane parallel FPC resonator, which performs the focusing function. In the previously mentioned FPC antenna, metal strips were used to make both reflecting mirrors. The mirror's strips and their slots are substantially smaller in size than the operational wavelength.

In general, metasurface (MS) layers have been used to design PRS functionalities in FPC antennas thanks to its unique characteristics [19, 20]. In [21], the MS is used to achieve beam steering in an FPC antenna at 2.25 GHz. A feeding source with a ground plane and a PRS-modulated MS make up the antenna's structure. The phase-modulated MS is attained by varying inductance of PRS and 30° beam steering is achieved. In [22], coding MS is introduced to create an FPC antenna with high gain by achieving low scattering from 8 to 12 GHz by re-emitting the EM waves in all directions without effect on the radiation characteristics. Two layers of square unit cells make up the coding MS and was printed on a dielectric material substrate. The upper one is used to structure coding MS while the bottom one is used as PRS. Also, MS can be used to design a linear to circular polarization FPC antenna as in [23]. An MS unit cell is consisting of two layers, a circular polarization patch as a top layer, and a linear polarization patch as a bottom layer in between a metallic plane exists. The two layers are connected by metallic via the FPC antenna operates over the band of frequency from 9.8 to 10.2 GHz with an aperture efficiency of 53%.

In [24], an MS layer made up of an aperiodic matrix of holes is designed by integrating a near-zero refractive index material with an FPC antenna to achieve wideband, high directivity, and high front-to-back ratio properties. Also, MS is used to realize the shrinking profile of the FPC antenna as introduced in [25]. The authors depend on reducing the height of the air gap between the layers of the FPC antenna by using stratified MS which acts as a PRS and using the slotted waveguide antenna as a feeding source. Hence, the profile is reduced to only half of the wavelength with a gain of 19.6 dBi at 19 GHz.

In [26], an MS is used to achieve a dual-polarized split beam at Ku-band. The reflecting MS unit cells are used as a sandwich in between the FPC antenna. The MS layer is composed of gradient MS at the top and periodic MS at the bottom. The top MS and bottom MS are linked to each other by cylinders cross vias on the superstrate. The introduced MS layer converts the linear waves from the feeding source (patch antenna) into left-hand circular polarization waves and right-hand circular polarization waves.

The goal of this article is to present a novel configuration of a highly reflective MS layer to increase the directivity and widen the bandwidth of an FPC antenna for 5G applications. It is noteworthy that the concept of this paper is published in brief by the authors in [27] and here the full work is presented. Full-wave EM simulations and measurements were used to verify the structure's performance. The structure of the paper is as follows: in Section "FPC antenna for increasing directivity," the theory analysis for increasing directivity of FPC antenna is analyzed, the design of highly reflective MS unit cell, and the behavior of FPC antenna is discussed. In Section "Fabrication and measurements," the fabrication and measurements results are introduced. This work's conclusion is summarized in Section "Conclusion."

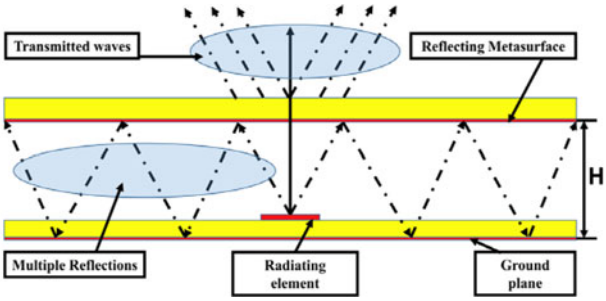

Fig. 1. Ray theory model of FPC antenna for increasing directivity.

FPC antenna for increasing directivity

The construction of the proposed FPC antenna consists of a grounded square patch antenna printed on an FR4 substrate as a primary radiating source and loaded with another ungrounded FR4 superstrate layer made up of a highly reflective MS layer whose unit cells are printed on the superstrate's bottom face, and an air cavity is sandwiched between the two layers. The MS layer which is set parallel to the antenna's ground plane layer will produce numerous reflections between the two layers which construct the proposed FPC antenna. The increase of the antenna directivity and hence its gain has been achieved thanks to the highly reflecting MS layer. In this section, we begin by explaining the design theory and analysis of the MS layer. Next, the detailed design procedures of the MS unit cell, MS layer, and the results are discussed in the next sub-sections.

Theory and analysis for increasing directivity of FPC antenna

The analysis of the FPC antenna can be explained based on ray tracing theory whose model is shown in Fig. 1. The multiple reflections within the cavity result in the antenna directivity enhancement in the boresight direction.

The directivity enhancement of the antenna in the normal direction is limited because the reflected waves between the PRS layer and the antenna may have out-of-phase characteristics.

It is worth noting that this phase difference is introduced by the phase variations of reflections from the highly reflecting MS and the antenna's ground plane and also the path differences between the reflected waves. Accordingly, the antenna power pattern is given as follows [28]:

$$P(\theta) = \frac{1 - R^2(\theta)}{1 + R^2(\theta) - 2R(\theta)\cos\left[\varphi(\theta) - \pi - (4\pi H/\lambda)\right]} F^2(\theta) \quad (1)$$

where θ is the angle of incidence of the PRS's reflected waves, $R(\theta)$ is the reflection amplitude, $\varphi(\theta)$ is the reflection phase, $F(\theta)$ is the primary source (microstrip patch) antenna's radiation pattern, H is the Fabry–Pérot antenna's height (the separation between the patch antenna ground and highly reflecting MS layer) (the superstrate bottom face), λ is a the free-space wavelength, and finally π is the reflection phase from the ground plane of the patch antenna.

Maximum power in the normal direction ($\theta = 0°$) and the in-phase reflected waves are obtained as:

$$\varphi(0) - \pi - \frac{4\pi H}{\lambda} = 2N\pi \quad \text{where } N = 0,\ 1,\ 2,\ \ldots \quad (2)$$

https://doi.org/10.1017/S1759078722001015 Published online by Cambridge University Press

Using (2), FPC antenna height H is set to achieve resonance as follows:

$$H = \left(\frac{\varphi(0)}{\pi} - 1\right)\frac{\lambda}{4} + N\frac{\lambda}{2} \quad \text{where } N = 0,\ 1,\ 2,\ \ldots \tag{3}$$

In (3), it has been shown that the gain maximization (phase quality) in free space in the normal direction is adjusted using the separation between the PRS layer and the antenna (H) adjustment. In other words, in the normal direction, the phase equality of the propagated waves outside of the MS PRS layer is adjusted using this separation distance (H). For the highly reflecting MS ($\varphi(0) \approx \pi$) [29]. From equation (3), the cavity height (for $N = 1$) is equal to $\lambda/2$. The exciting mode of the cavity is the second mode ($N = 1$).

The boresight directivity of the FPC antenna with respect to the traditional feeding patch antenna can be computed as follows [30], assuming the size of the resonant cavity is infinite:

$$D_r = 10\log\left(\frac{1+R}{1-R}\right) \tag{4}$$

where D_r is the relative directivity of the FPC antenna and R is the reflection magnitude of a highly reflecting MS unit cell. From (4), it can be deduced that R should be increased to achieve an FPC antenna with high directivity as possible. As discussed in the next section, the reflection magnitude of the highly reflecting MS unit cell is about 0.932 at 28 GHz. So, by using equation (4), the relative directivity of the FPC antenna will be 14.4 dBi.

The directivity of the proposed FPC antenna will be:

$$D = D_r + D_f \tag{5}$$

where D_f is the directivity of the traditional feeding patch antenna and D_r is the relative directivity that is calculated by equation (4). The directivity of the traditional feeding patch antenna is about 6 dBi thus, by using equation (5), the directivity of the proposed FPC antenna is 20.4 dBi.

Highly reflecting MS unit cell

The design procedure for synthesizing a general MS unit cell for a specific function can be found in [31]. The unit cell is divided into lattices marked with "0" or "1." The lattice marked with "0" means the area is free from the copper while the lattice which is marked with "1" means the area is covered with a copper layer. Applying this method, our proposed unit cell has been encoded in a matrix. To reduce the number of matrix and coding processes, the unit cell has been selected to be symmetric along the x-axis and y-axis. The unit cell has been developed through the following shapes as shown in Fig. 2(a). The relevant S-parameters and the transmission phase of each unit cell are shown in Figs 2(b) and 2(c), respectively. The main design objective for these unit cells is to be small in order or half-wavelength. In the first unit cell, the resonance frequency is 31.1 GHz which is greater than the required frequency so the unit cell is modified to the second unit cell to reduce the frequency which is 29.4 GHz which in turn leads to the third unit cell. Once the MS unit cell shape was designed, the best values of dimensions are obtained by the parametric study using the available EM simulator. The

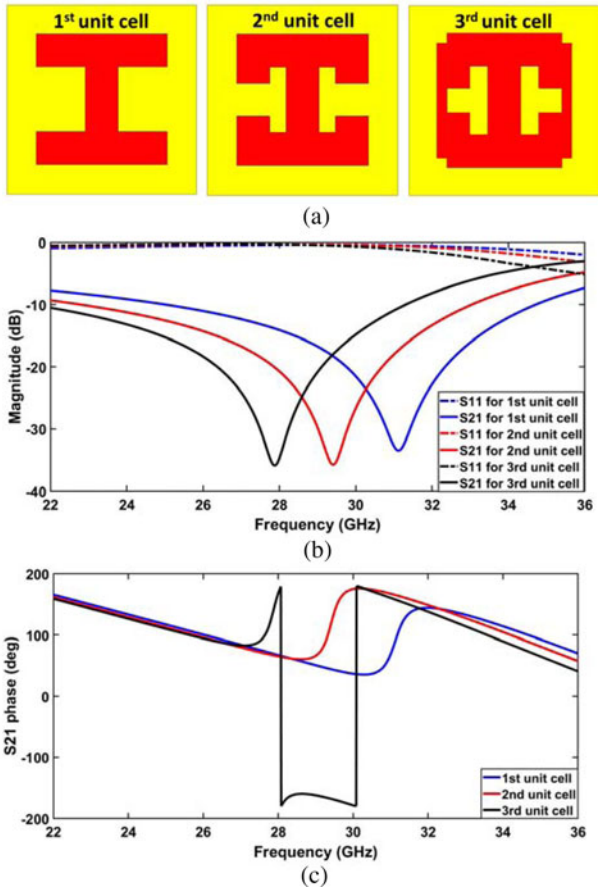

Fig. 2. (a) Shapes of developing highly reflecting MS unit cells, (b) simulated S_{11} and S_{21} parameters of the MS unit cells, and (c) the simulated S_{21} phase of the MS unit cells.

cell shape selection is explained here, and its optimization process will be discussed later.

The goal of designing a highly reflective MS in our case is to maximize the difference between the transmission coefficient (S_{21}) and the reflection coefficient (S_{11}) so that all the energy is transmitted through the air cavity with minimal reflections. The unit cell's phase should be zero at the resonance frequency and there is a 180° change in phase as mentioned in [32, 33].

The proposed high reflective MS unit cell's detailed geometry is presented in Fig. 3. In this construction, an FR4 dielectric material of 0.8 mm thick and with a relative permittivity of 4.4 was used. The commercial ANSYS HFSS was used to model the

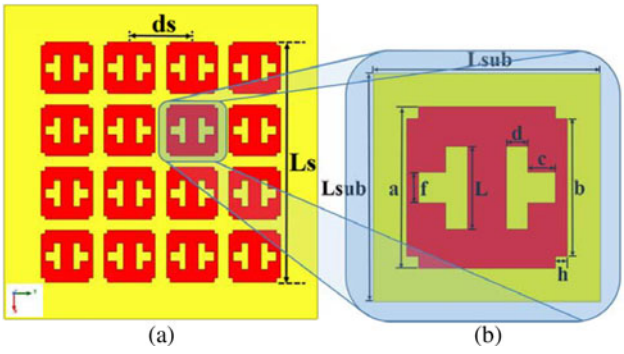

Fig. 3. Geometry of the highly reflecting MS unit cell.

https://doi.org/10.1017/S1759078722001015 Published online by Cambridge University Press

Table 1. Dimensions of MS unit cell

Cell parameter	Dimensions (mm)	Cell parameter	Dimensions (mm)
a	0.5	b	2.9
c	2.1	d	1.2
h	0.3	L	1.2
f	1.2	L_{sub}	1.2
L_s	19.1	d_s	5

MS unit cell with perfect electric boundaries and magnetic boundaries on the y-axis and x-axis, respectively, to simulate the infinite periodic structure. The illustration of dimensions of the introduced MS unit cell is depicted in Table 1.

The simulated transmission coefficient (S_{21}) and reflection coefficient (S_{11}) are shown in Fig. 4 (right y-axis). According to the results, the difference between the magnitudes of the S_{11} and S_{21} coefficients are largest at 28 GHz with a value of 34.3 dB. In addition, the MS unit cells' S_{21} coefficient phase is given in Fig. 3 (left y-axis) which shows that the high-directive FPC antenna has a near-zero transmission phase at the resonance frequency (28 GHz) and there is a phase jump from 180 to −180° at 28 GHz.

To discuss ohmic and dielectric losses and their influence on S-parameters of the MS unit cell, the simulation was performed in ANSYS HFSS by regarding the MS unit cell as a perfect electric conductor and assuming the FR4 substrate as having no losses. The results are plotted in Fig. 5 which demonstrate that the value of the S_{21} coefficient decreased and also the resonant frequency is shifted to 27.8 GHz and also the difference between the S_{21} and S_{11} coefficients at 27.8 GHz becomes 69.7 dB while in the previous case the difference was 35.4 and 34.3 dB at 27.8 and 28 GHz, respectively. The reason behind the difference between the results of Figs 4 and 5 is ohmic and dielectric losses.

The high-gain MS-based FPC antenna

The geometry of the introduced high directivity MS-based FPC antenna is depicted in Fig. 6. An array of 4 × 4 unit cells make up the MS superstrate layer which is shown in Fig. 3(a). The dielectric substrates of the patch antenna and the MS are FR-4 with $h_{\text{sub}} = 0.8$ mm and $\varepsilon_r = 4.4$. The overall FPC antenna dimensions are $25 \times 25 \times 6.265$ mm^3. It is worth commenting that the cavity height is half-wavelength at 28 GHz.

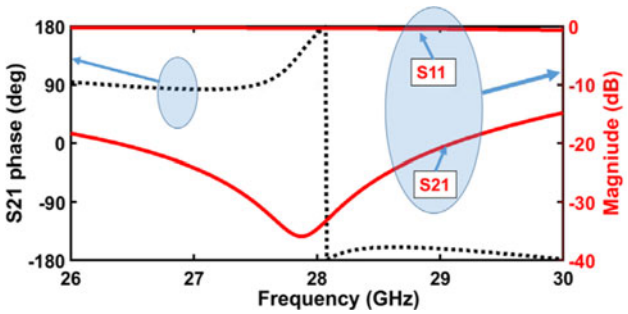

Fig. 4. Simulated S_{11} and S_{21} parameters of the MS unit cell (right axis) and simulated S_{21} phase of the proposed unit cell (left axis).

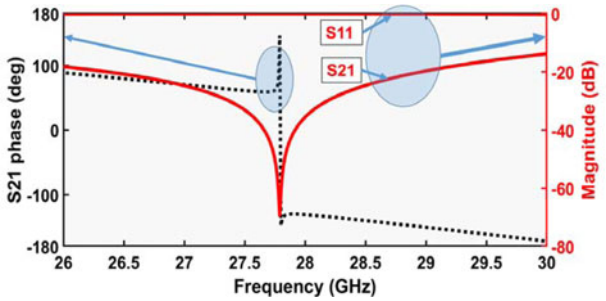

Fig. 5. Simulated results of a PEC MS unit cell with a lossless dielectric substrate, S_{11} and S_{21} parameters (right axis) and phase of S_{21} for the cell (left axis).

The simulated reflection coefficients (S_{11}) versus frequency for both the microstrip patch antenna and the proposed MS-based FPC antenna are plotted in Fig. 7. The simulated results illustrate that the S_{11} coefficient of the patch antenna is less than −10 dB over a band of frequency from 27.6 to 28.6 GHz (1 GHz absolute bandwidth and fractional bandwidth of 3.5%) with a maximum

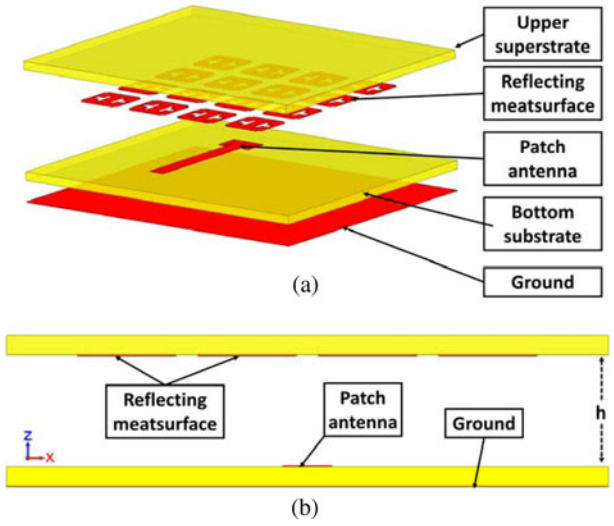

Fig. 6. Geometry of the MS-based FPC antenna: (a) the prospective layers view and (b) the side view.

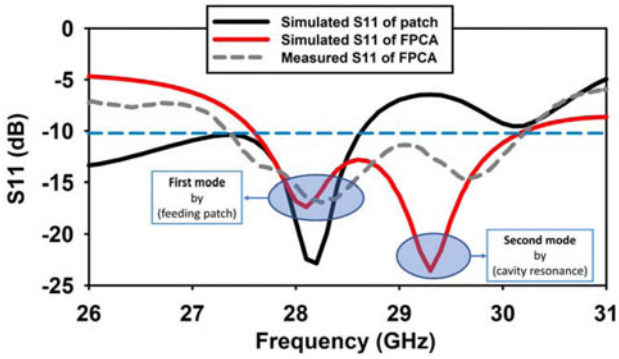

Fig. 7. Simulated and measured reflection coefficient (S_{11}) of the microstrip antenna and the MS layer-based FPC antenna.

https://doi.org/10.1017/S1759078722001015 Published online by Cambridge University Press

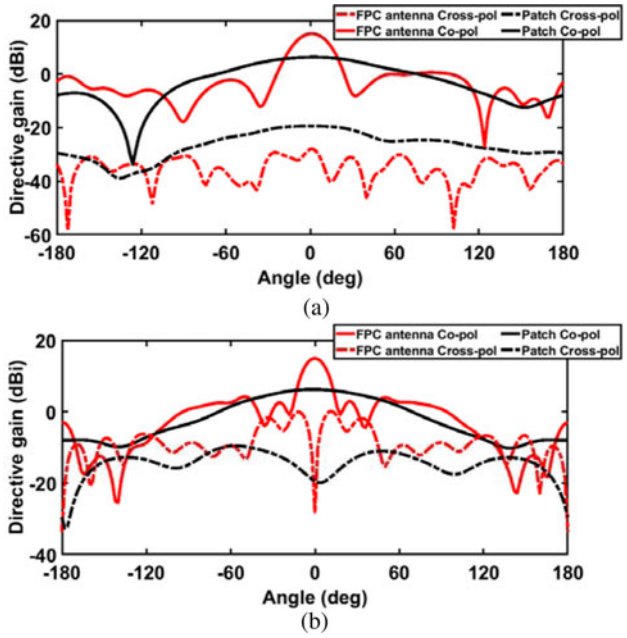

Fig. 8. Simulated two-dimensional radiation pattern of the MS layer-based FPC antenna and patch antenna at 28 GHz: (a) *E*-plane and (b) *H*-plane.

resonance value of S_{11} coefficient equals −23 dB at 28.1 GHz. In the case of the MS-based FPC antenna, the antenna maintains its main resonance at 28.1 GHz of the main radiating microstrip patch at 28.15 GHz and a reflection coefficient equals −17 dB.

In addition to this resonance, a second resonance at 29.6 GHz whose S_{11} value is −15 dB is noted, which can be claimed as a result of the cavity resonance demonstrated earlier in Fig. 1. The S_{11} bandwidth of −10 dB of the proposed MS-based FPC antenna has become wider, compared to the microstrip patch antenna, of frequency from 27.6 to 30.2 GHz. In other words, this means that the absolute bandwidth of the FPC antenna equals 2.6 GHz (almost 9% fractional bandwidth). In other words, it is possible to claim that the proposed FPC antenna has nearly three times the bandwidth of the microstrip patch antenna.

It can be observed that there are two resonances for the FPC antenna: the first resonance is achieved by the feeding microstrip antenna and the second mode is achieved by the cavity resonance which is mainly governed by cavity height.

The simulated co-polarization and cross-polarization radiation patterns in both the *E*-plane and *H*-plane at the resonance frequency (28 GHz) for both the microstrip patch antenna and the MS-based FPC antenna are plotted in Figs 8(a) and 8(b),

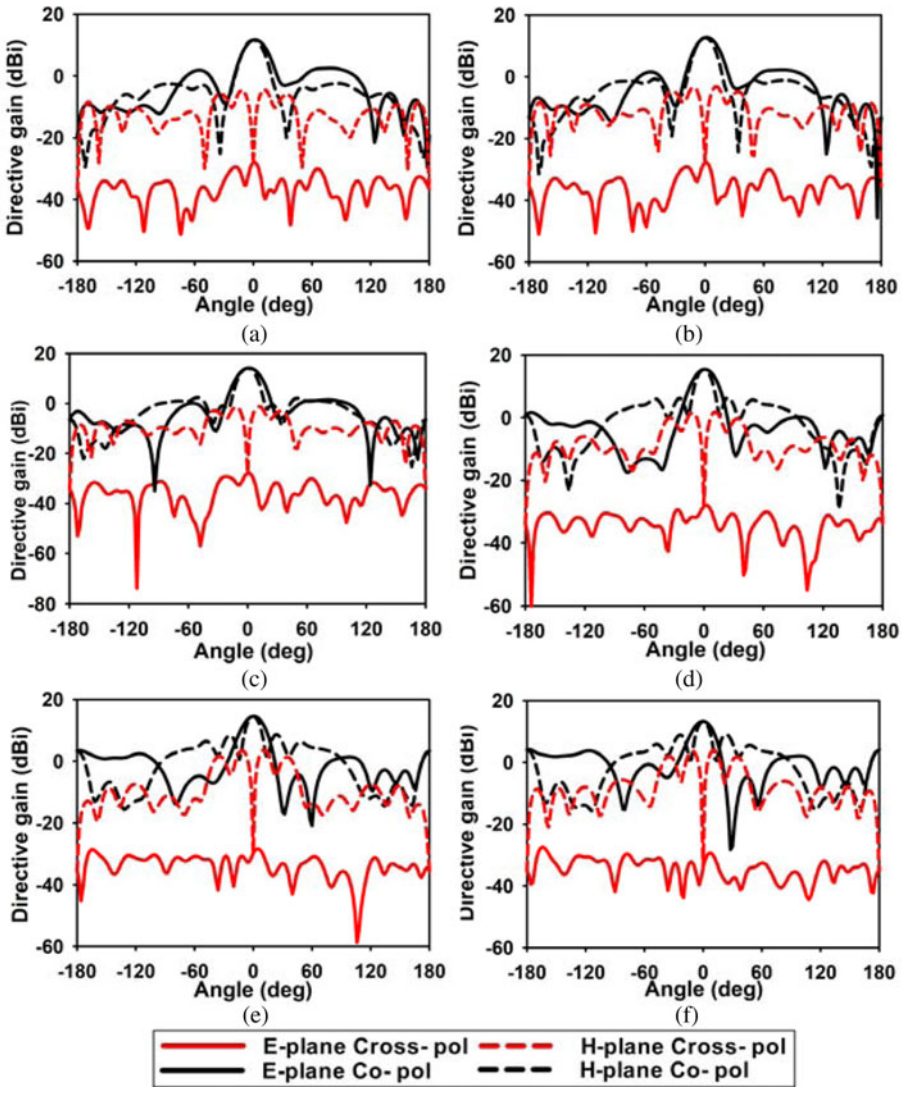

Fig. 9. Simulated *E*-plane and *H*-plane co-polarization and cross-polarization radiation patterns of the FPC antenna at (a) 27.3 GHz, (b) 27.5 GHz, (c) 27.8 GHz, (d) 28.3 GHz, (e) 28.7 GHz, and (f) 29 GHz.

https://doi.org/10.1017/S1759078722001015 Published online by Cambridge University Press

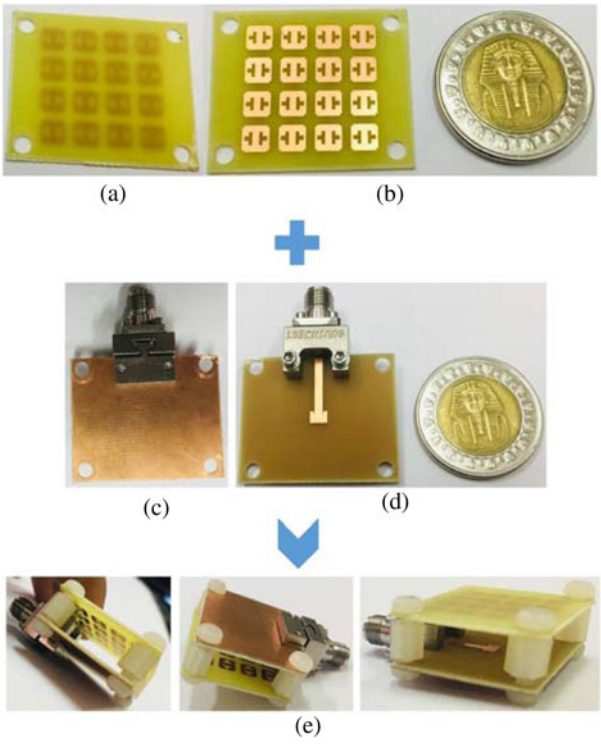

Fig. 10. Fabricated FPC antenna: (a) top view of highly reflecting MS, (b) bottom view of highly reflecting MS, (c) ground plane, (d) feeding source, and (e) 3D configuration of the fabricated antenna.

respectively. The directivity of the microstrip patch antenna is 6 dBi at a boresight angle and the directivity increases to 15 dBi when the highly reflective MS unit cells were inserted into the FPC antenna. This means, there is a 9 dBi enhancement in the directivity of the FPC antenna and the radiation efficiency of the introduced FPC antenna is 56%, while the aperture efficiency of 47%.

The co-polarization and the cross-polarization radiation patterns of the proposed MS-based FPC antenna in the *E*-plane and *H*-plane at different extreme frequencies are shown in Fig. 9 to demonstrate the directivity enhancement and radiation properties of our FPC antenna over a wideband. As shown in the figure, it is obvious that the maximum value of the co-polarized pattern at the boresight direction is 11.7 dBi for 27.3 GHz, 12.8 dBi for 27.5 GHz, 14.2 dBi for 27.8 GHz, 15.45 dBi for 28.3 GHz, 14.6 dBi for 28.7 GHz, and 13.4 dBi for 29 GHz. It can be observed that the 3 dB beamwidth of the co-polarized pattern is 24° for 27.3 GHz, 23° for 27.5 and 27.8 GHz, 22° for 28.3 GHz, 21° for 28.7 GHz, and 20° for 29 GHz which confirms that the designed FPC antenna has high-directive properties. In the boresight direction, the cross-component is very low (close to −40 dB in the *E*-plane). As the beam becomes wider, the cross-polarized component becomes higher in the sidelobes of the antenna in the *H*-plane. While in the *E*-plane, the cross-polarized component is still in the order of −40 dB for all beam angles.

Fabrication and measurements

The fabricated antenna prototype from different perspective views and fabrication layer details are shown in Fig. 10. The antenna has

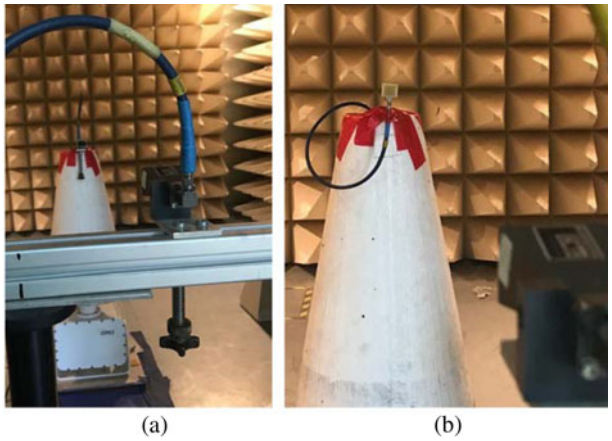

Fig. 11. Measurement setup of directive gain of fabricated FPC antenna: (a) two standard horn antennas (transmitting antenna and reference antenna) and (b) replacing reference antenna by the AUT.

one superstrate layer; the bottom of the superstrate layer is a highly reflecting MS for increasing the gain as shown in Figs 10(a) and 10(b). The highly reflecting MS is designed as 4 × 4 planar arrays. The superstrate and the microstrip patch antenna employ a lost cost FR4 substrate with a 0.8 mm thickness and a 4.4 dielectric constant. In Figs 10(c) and 10(d), the microstrip patch antenna substrate has a ground plane of dimensions 25 mm × 25 mm ($2.33\lambda \times 2.33\lambda$ at 28 GHz). The superstrate's overall dimensions are 25 mm × 25 mm which can be noticed by comparing the antenna size with a coin. As deduced in Section "FPC antenna for increasing directivity," the separation between the feeding substrate and the superstrate is half-wavelength. Four nylon screws with the same height of the cavity are used to fix the FPC antenna.

As shown in Fig. 7, the measured reflection coefficient (S_{11}) of the fabricated FPC antenna has a bandwidth of lower than −10 dB within the frequency band (27.3–30.2 GHz, a bandwidth of 2.9 GHz). These measured results agree to a high level with the results of a simulation that is presented in Fig. 7 and confirm the properties of the wide bandwidth. The small disparities between the simulated and measured results can be related to the non-voided imperfection in either fabrication, measurements, or both.

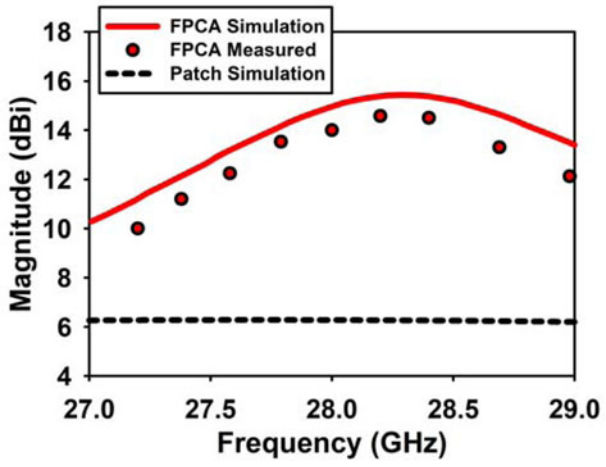

Fig. 12. Simulated and measured gains of the FPC antenna.

https://doi.org/10.1017/S1759078722001015 Published online by Cambridge University Press

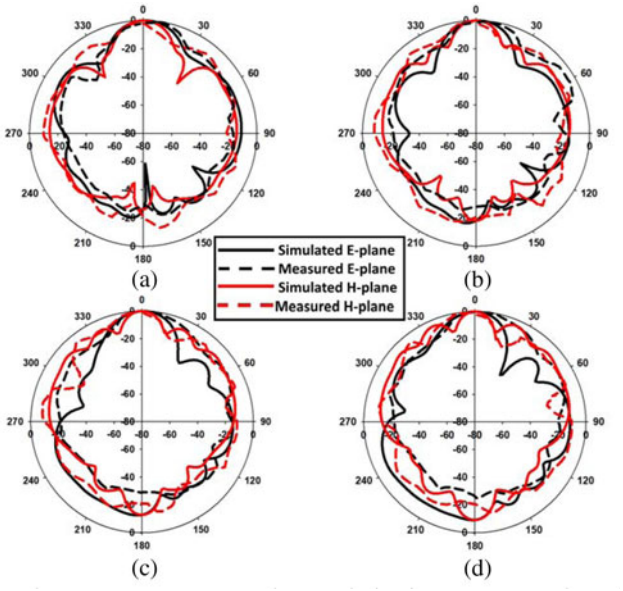

Fig. 13. Normalized measured cross-polarization *E*-plane and *H*-plane radiation patterns of the FPC antenna at (a) 27.5 GHz, (b) 28 GHz, (c) 28.5 GHz, and (d) 29 GHz.

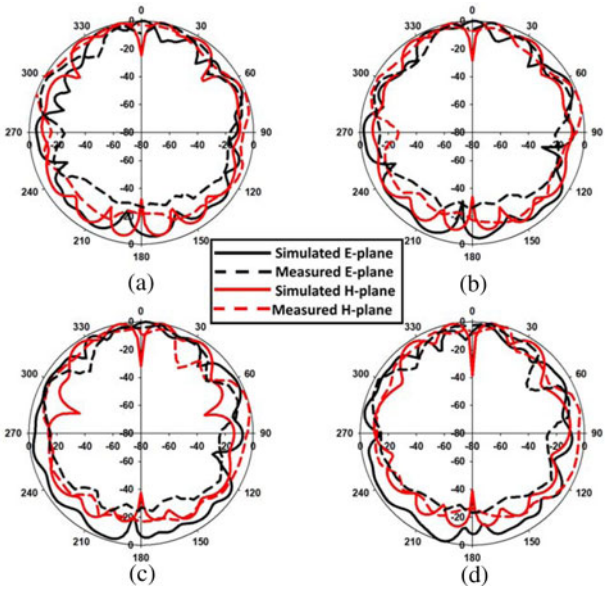

Fig. 14. Normalized measured co-polarization *E*-plane and *H*-plane radiation patterns of the FPC antenna at (a) 27.5 GHz, (b) 28 GHz, (c) 28.5 GHz, and (d) 29 GHz.

The gain of the fabricated high-gain FPC antenna was measured by using two standard horn antennas and Vector Network Analyzer (VNA), one horn is used as a transmitting antenna at port 1 and the second horn as a reference antenna at port 2 with a separating distance of 1 m (to be in the far-field region) as shown in Fig. 11(a). Then, the transmission coefficient (S_{21}) is measured with a reference antenna. The second step, as shown in Fig. 11(b), is to replace the reference antenna with the fabricated FPC antenna (Antenna Under Test (AUT)) with a separating distance of 1 m from the transmitting antenna and S_{21} is measured by using Antenna Under Test (AUT). To obtain the value of the gain the two S_{21} coefficients are subtracted, and the obtained result is the gain of the fabricated FPC antenna.

In Fig. 12, the proposed antenna gains (simulated and measured antenna results) are plotted. The simulated peak gain is 15.46 dBi at 28.3 GHz, while the simulated 3 dB gain bandwidth range is from 27.4 to 29.3 GHz, which agrees well with the impedance bandwidth shown in Fig. 7. On the other hand, the maximum measured gain of the fabricated FPC antenna is 14.3 dBi at 28.3 GHz with the 3 dB gain bandwidth from 27.6 to 29 GHz. The reduction of antenna gains in measurement compared to the simulation can be claimed due to the accumulation of different dielectric/conduction losses in the measurement process. Besides, the aligment tolerance error which in the process of combining the antenna with the superstrate.

In Figs 13(a)–13(d), the measured co-polarized antenna directive gain patterns of the fabricated MS-based FPC antenna in both the *E*-plane and *H*-plane are plotted at different frequencies over the operating bandwidth frequencies: 27.5, 28, 28.5, and 29 GHz (compared with simulation results). As shown in the figure, in both planes, the main lobe of the radiation pattern is at zero degrees which is the boresight direction at all frequencies. Also, the sidelobe levels are almost equal at 27.5 and 28 GHz in the *H*-plane; however, it becomes slightly higher in the *E*-plane at 28.5 and 29 GHz. It is worth mentioning that the measured pattern is good but non-ideal as a simulation as a result of the available measurement scenario.

Also, the measured cross-polarized antenna directive gain patterns of the fabricated antenna in both the *E*-plane and *H*-plane are plotted at different frequencies over the operating bandwidth frequencies: 27.5, 28, 28.5, and 29 GHz as shown in Fig. 14. The comparison between the simulated cross-polarization component and measured cross-polarization component is also shown. As can be deduced from Fig. 14, the measured cross-polarization patterns for both *E*-plane and *H*-plane are in good agreement with the simulation results.

Finally, based on the literature, it has been concluded that there is still room for achieving high directivity side-by-side with a low profile and bandwidth. So comparing the performance of the introduced FPC antenna versus the previous work is illustrated in Table 2. As can be seen in [5, 34], its relevant antennas had a smaller bandwidth (2.7 and 4.28%) besides smaller gain (2.3 and 7.65 dBi) than the proposed work. And then, in [35], the gain of the antenna was increased to 6.6 dBi with 10% bandwidth. The gain is increased in [36, 37] to 13.5 and 10.2 dBi, respectively, with the same bandwidth of [35] besides the increase in the gain was realized at the expense of increasing the size which is almost $3\lambda \times 3\lambda$ (which is large size). In order to increase the bandwidth, in [38] and [7], 16.58 and 30% bandwidth were achieved at the expense of low gain (4.6 and 6.95 dBi). In [39], bandwidth was increased to 29.3% with a low profile ($1.75\lambda \times 1.75\lambda$) and with reasonable directivity of 11.45 dBi; however, the main radiator is an Magneto-Electric (ME) dipole which requires a large height which is unpractical for some applications. Next in [42, 43], the gain was increased to 13.78 and 12.64 dBi, respectively, and the bandwidth was also improved (15.5 and 19.2%, respectively). However, the antenna cavity thickness was increased to 0.6λ and 0.65λ (30% increase compared to 0.5%) which means the improvements of the gain and the bandwidth were at the expense of the cavity height and the overall size ($3\lambda \times 3\lambda$ and $2.55\lambda \times 2.55\lambda$). There are also a trivial solution to increase the bandwidth and the gain by increasing the number of the MS superstrate layers as in [11, 40, 41] which results in a very large

https://doi.org/10.1017/S1759078722001015 Published online by Cambridge University Press

Table 2. Comparison between the introduced antenna and recently published work

Ref.	Operating band (GHz) and the main (radiating source)	Separation of superstrate	Peak gain (dBi)	Numbers of superstrates	Overall planar dimensions	Impedance bandwidth (%)	Aperture efficiency (%)
[5]	5.71–5.87 (patch)	0.386λ	2.3	1	NA	2.7	NA
[34]	5.14 (patch)	0.6λ	7.65	1	NA	4.28	NA
[35]	9.7–10.4 (patch)	NA	6.6	1	2.04λ × 2.04λ	10.8	NA
[36]	11.7–12.9 (patch)	0.942λ	13.5	1	2.97λ × 2.97λ	10.1	39.4
[37]	10.5–10.7 (patch)	0.5λ	10.2	1	3.03λ × 3.03λ	1.88	NA
[38]	9.4–11.3 (patch)	NA	4.9	1	2.20λ × 2.20λ	16.58	57.4
[7]	10 (patch)	0.5λ	6.95	1	NA	30	NA
[39]	15 (ME dipole)	0.5λ	11.45	1	1.75λ × 1.75λ	29.3	36
[11]	8.8–11 (patch)	NA	13.8	2	NA	NA	NA
[40]	13–14.5 (slot)	0.6λ	16.9	3	NA	10.9	NA
[41]	8.8–11.3 (patch)	0.8λ	14	2	NA	25	NA
[42]	12.6–15.2 (slot)	0.6λ	13.78	1	3λ × 3λ	15.5	NA
[43]	10.3–12.5 (slot)	0.65λ	12.64	1	2.55λ × 2.55λ	19.2	NA
[44]	12.95–13.95 (patch)	NA	17.2	1	2.28λ × 2.28λ	7.4	NA
Proposed antenna	**26.65–29.7 (patch)**	**0.46λ**	**14.3**	**1**	**2.33λ × 2.33λ**	**10.09**	**46**

profile. Finally, we can conclude that the proposed antenna has the greatest bandwidth with more suitable size and better gain.

Conclusion

For 5G applications, a highly reflective MS is employed to increase the directivity/gain of the FPC antenna and to also provide a wide bandwidth. The design goals are achieved using a 4 × 4 MS superstrate layer array so that the overall size is 25 mm × 25 mm (2.33λ × 2.33λ at 28 GHz). The bandwidth is lower than −10 dB from 27.6 to 30.2 GHz. The microstrip patch antenna's fractional bandwidth is 3.5%, whereas the proposed MS-based FPC antenna's fractional bandwidth is 9% (nearly three times wider). The fabricated MS-based FPC has a bandwidth of lower than −10 dB from 27.3 to 30.2 GHz. The simulated maximum gain is 15.46 dBi at 28.3 GHz, with a 3 dB bandwidth from 27.4 to 29.3 GHz. While in the measurement case, the peak gain is 14.3 dBi at 28.3 GHz with a 3 dB bandwidth of gain from 27.6 to 29 GHz.

References

1. **Liu ZG, Cao ZX and Wu LN** (2016) Compact low-profile circularly polarized Fabry–Perot resonator antenna fed by linearly polarized microstrip patch. *IEEE Antennas and Wireless Propagation Letters* **15**, 524–527.
2. **Akalin T, Danglot J, Vanbesien O and Lippens D** (2002) A highly directive dipole antenna embedded in a Fabry–Perot type cavity. *IEEE Microwave and Wireless Components Letters* **12**, 48–50.
3. **Feresidis A, Goussetis G, Wang S and Vardaxoglou J** (2005) Artificial magnetic conductor surfaces and their application to low-profile high gain planar antennas. *IEEE Transactions on Antennas and Propagation* **53**, 209–215.
4. **Sun Y, Chen ZN, Zhang YW, Chen H and See TSP** (2012) Subwavelength substrate-integrated Fabry–Pérot cavity antennas using artificial magnetic conductor. *IEEE Transactions on Antennas and Propagation* **60**, 30–35.
5. **Kim JH, Ahn CH and Bang JK** (2016) Antenna gain enhancement using a holey superstrate. *IEEE Transactions on Antennas and Propagation* **64**, 1164–1167.
6. **Li D, Szabo Z, Qing X, Li EP and Chen ZN** (2012) A high gain antenna with an optimized metamaterial inspired superstrate. *IEEE Transactions on Antennas and Propagation* **60**, 6018–6023.
7. **Kurra L, Abegaonkar MP, Basu A and Koul SK** (2016) FSS properties of a uniplanar EBG and its application in directivity enhancement of a microstrip antenna. *IEEE Antennas and Wireless Propagation Letters* **15**, 1606–1609.
8. **Kumar S, Kurra L, Abegaonkar M, Basu A and Koul SK** (2015) Multilayer FSS for gain improvement of a wide-band stacked printed antenna. *International Symposium on Antennas and Propagation (ISAP)*, Hobart, TAS, 1–4.
9. **Augustin G, Chacko BP and Denidni TA** (2013) A zero-index metamaterial unit-cell for antenna gain enhancement. *IEEE Antennas and Propagation Society International Symposium (APSURSI)*, Orlando, 126-127.
10. **Zeb BA, Ge YH, Esselle KP, Sun Z and Tobar ME** (2012) A simple dual-band electromagnetic band gap resonator antenna based on inverted reflection phase gradient. *IEEE Transactions on Antennas and Propagation* **60**, 4522–4529.
11. **Wang NZ, Liu Q, Wu CY, Talbi L, Zeng Q and Xu J** (2014) Wideband Fabry–Perot resonator antenna with two complementary FSS layers. *IEEE Transactions on Antennas and Propagation* **62**, 2463–2471.
12. **Muhammad SA, Sauleau R and Legay H** (2012) Small-size shielded metallic stacked Fabry–Perot cavity antennas with large bandwidth for space applications. *IEEE Transactions on Antennas and Propagation* **60**, 792–802.
13. **Zeb BA, Nikolic N and Esselle KP** (2015) A high-gain dual-band EBG resonator antenna with circular polarization. *IEEE Antennas and Wireless Propagation Letters* **14**, 108–111.
14. **Ma XL, Huang C, Pu M, Hu CG, Feng Q and Luo XG** (2012) Single layer circular polarizer using metamaterial and its application in antenna. *Microwave and Optical Technology Letters* **54**, 1770–1774.
15. **Konstantinidis K, Feresidis AP and Hall PS** (2014) Dual subwavelength Fabry–Perot cavities for broadband highly directive antennas. *IEEE Antennas and Wireless Propagation Letters* **13**, 1184–1186.

https://doi.org/10.1017/S1759078722001015 Published online by Cambridge University Press

16. **Guzman-Quiros R, Gomez-Tornero JL, Weily AR and Guo YJ** (2012) Electronic full-space scanning with 1-D Fabry–Pérot LWA using electromagnetic band-gap. *IEEE Antennas and Wireless Propagation Letters* **11**, 1426–1429.
17. **Guzman-Quiros R, Gomez-Tornero JL, Weily AR and Guo YJ** (2012) Electronically steerable 1-D Fabry–Perot leaky-wave antenna employing a tunable high impedance surface. *IEEE Transactions on Antennas and Propagation* **60**, 5046–5055.
18. **Sauleau R, Coquet P, Matsui T and Daniel J-P** (2003) A new concept of focusing antennas using plane-parallel Fabry–Perot cavities with non-uniform mirrors. *IEEE Transactions on Antennas and Propagation* **51**, 3171–3175.
19. **Singh AK, Abegaonkar MP and Koul SK** (2019) Wide gain enhanced band high gain Fabry–Perot cavity antenna using ultrathin reflecting metasurface. *Microwave and Optical Technology Letters* **61**, 1628–1633.
20. **Ratni B, Merzouk WA, Lustrac AD, Villers S, Piau GP and Burokur SN** (2017) Design of phase-modulated metasurfaces for beam steering in Fabry–Perot cavity antennas. *IEEE Antennas and Wireless Propagation Letters* **16**, 1401–1404.
21. **Ratni B, Merzouk WA, de Lustrac A, Villers S, Piau G and Burokur SN** (2017) Design of phase-modulated metasurfaces for beam steering in Fabry–Perot cavity antennas. *IEEE Antennas and Wireless Propagation Letters* **16**, 1401–1404.
22. **Zhang L, Wan X, Liu S, Yin JY, Zhang Q, Wu HT and Cui TJ** (2017) Realization of low scattering for a high-gain Fabry–Perot antenna using coding metasurface. *IEEE Transactions on Antennas and Propagation* **65**, 3374–3383.
23. **Xie P, Wang G, Li H, Liang J and Gao X** (2020) Circularly polarized Fabry–Perot antenna employing a receiver–transmitter polarization conversion metasurface. *IEEE Transactions on Antennas and Propagation* **68**, 3213–3218.
24. **Dawar P and Abdalla MA** (2021) Near-zero-refractive-index metasurface antenna with bandwidth, directivity and front-to-back radiation ratio enhancement. *Journal of Electromagnetic Waves and Applications* **35**, 1863–1881.
25. **Deng F and Qi J** (2020) Shrinking profile of Fabry–Perot cavity antennas with stratified metasurfaces: accurate equivalent circuit design and broadband high-gain performance. *IEEE Antennas and Wireless Propagation Letters* **19**, 208–212.
26. **Yang P, Yang R and Li Y** (2021) Dual circularly polarized split beam generation by a metasurface sandwich-based Fabry–Pérot resonator antenna in Ku-band. *IEEE Antennas and Wireless Propagation Letters* **20**, 933–937.
27. **El-Sewedy MF, Abdalla MA and Elregely HA** (2020) High directive Fabry–Pérot cavity antenna by using reflecting metasurface for 5G applications. 2020 *IEEE AP-S International Antenna and Propagation Symposium Digest*, Montreal, Canada, 817–818.
28. **Trentini GV** (1956) Partially reflecting sheet arrays. *IRE Transactions on Antennas and Propagation* **4**, 666–671.
29. **Chanimool S, Chung K and Akkaraekthalin P** (2010) Bandwidth and gain enhancement of microstrip patch antennas using reflective metasurface. *IEICE Transactions on Communications* **93**, 2496–2250.
30. **Xie P, Wang G, Li H and Gao X** (2019) A novel methodology for gain enhancement of the Fabry–Pérot antenna. *IEEE Access* **7**, 176170–176176.
31. **Qiu T, Shi X, Wang J, Li Y, Qu S, Cheng Q, Cui T and Sui S** (2019) Deep learning: a rapid and efficient route to automatic metasurface design. *Advancement of Science* **6**, 1900128.
32. **Hussain N, Jeong MJ, Park J and Kim N** (2019) A broadband circularly polarized Fabry–Perot resonant antenna using a single-layered PRS for 5G MIMO applications. *IEEE Access* **7**, 42897–42907.
33. **Singh AK, Abegaonkar MP and Koul S** (2017) High-gain and high-aperture-efficiency cavity resonator antenna using metamaterial superstrate. *IEEE Antennas and Wireless Propagation Letters* **16**, 2388–2391.
34. **Suthar H, Sarkar D, Saurav K and Srivastava KV** (2015) Gain enhancement of microstrip patch antenna using near-zero index metamaterial (NZIM) lens. *Twenty First National Conference on Communications (NCC)*, Mumbai, 1–6.
35. **Li W, Cao X, Gao J, Zhang Z and Cong L** (2016) Broadband RCS reduction and gain enhancement microstrip antenna using shared aperture artificial composite material based on quasi-fractal tree. *IET Microwaves, Antennas & Propagation* **10**, 370–377.
36. **Lv Y, Ding X and Wang B** (2020) Dual-wideband high-gain Fabry–Perot cavity antenna. *IEEE Access* **8**, 4754–4760.
37. **Ren J, Jiang W, Zhang K and Gong S** (2018) A high-gain circularly polarized Fabry–Perot antenna with wideband low-RCS property. *IEEE Antennas and Wireless Propagation Letters* **17**, 853–856.
38. **Zheng Y, Gao J, Zhou Y, Cao X, Yang H, Li S and Li T** (2018) Wideband gain enhancement and RCS reduction of Fabry–Perot resonator antenna with chessboard arranged metamaterial superstrate. *IEEE Transactions on Antennas and Propagation* **66**, 590–599.
39. **Cao W, Lv X, Wang Q, Zhao Y and Yang X** (2019) Wideband circularly polarized Fabry–Perot resonator antenna in Ku-band. *IEEE Antennas and Wireless Propagation Letters* **18**, 586–590.
40. **Konstantinidis K, Feresidis AP and Hall PS** (2015) Broadband subwavelength profile high-gain antennas based on multi-layer metasurfaces. *IEEE Transactions on Antennas and Propagation* **63**, 423–427.
41. **Wang N, Talbi L, Zeng Q and Xu J** (2018) Wideband Fabry–Perot resonator antenna with electrically thin dielectric superstrates. *IEEE Access* **6**, 14966–14973.
42. **Meriche MA, Attia H, Messai A, Mitu SSI and Denidni TA** (2019) Directive wideband cavity antenna with single-layer meta-superstrate. *IEEE Antennas and Wireless Propagation Letters* **18**, 1771–1774.
43. **Long M, Jiang W and Gong S** (2018) RCS reduction and gain enhancement based on holographic metasurface and PRS. *IET Microwaves, Antennas & Propagation* **12**, 931–936.
44. **Liu Z and Lu W** (2017) Low-profile design of broadband high gain circularly polarized Fabry–Perot resonator antenna and its array with linearly polarized feed. *IEEE Access* **5**, 7164–7172.

Mohamed F. El-Sewedy was born in 1992. He received his B.Sc. degree in electrical engineering from the Electrical Engineering Department, Military Technical College, Cairo, Egypt in 2016. He has joined Technical Research Centre in 2017. He is a member of the researchers' group in the electronic engineering department. He is currently pursuing an M.Sc. degree from the Electrical Engineering Department, Military Technical College, Cairo, Egypt. El-Sewedy currently a student member of the IEEE since 2020. His research interest includes metasurface antennas, millimeter antennas, characterization of EBG and mutual coupling reduction, MIMO antennas, radar deception targets, and finally, generation of electromagnetic pulse (EMP) and the protection from it.

Mahmoud Abdalla was born in 1973. He received his B.Sc. degree in electrical engineering from the Electrical Engineering Department, Military Technical College, Cairo, Egypt in 1995. He was awarded the M.Sc. degree in electrical engineering from Military Technical College in 2000, and the Ph.D. degree from Microwave and Communication Group, School of Electrical Engineering, Manchester University, UK in 2009. He has been with Military Technical College since 1996 where he is now a professor, the head of the Department Council Committee, and also the electromagnetic waves/microwave group in the Electronic Engineering Department. Also, he has been a Visiting Professor in the Department of Computer and Electrical Engineering, University of Waterloo, Canada since 2017. Prof. Abdalla is currently a senior member of the IEEE since 2015, URSI since 2020, and the European Microwave Association EuMA since 2011. He is a recognized international authority in the society of electromagnetics. He has published more than 200 peer-reviewed journal and conference papers. His research focuses on miniaturized multiband antennas/wideband microwave/millimeter components and antennas with great attention is to employ metamaterial/EBG, structures, MIMO antennas, energy harvesting systems, smart antennas, frequency selective surfaces, radar absorbers, and electromagnetic launchers. He is currently an

https://doi.org/10.1017/S1759078722001015 Published online by Cambridge University Press

editor and a reviewer in many electromagnetic journals such as *IEEE Transactions on Antenna and Propagation*, *IEEE Antennas and Wireless Propagation Letters*, *IEEE Transactions in Microwave Theory & Techniques*, *IEEE Microwave Wireless Components Letters*, *IEEE Transactions in Magnetics*, *IET Microwaves, Antenna and Propagation*, *IET Electronics Letters*, *IET Communications*, *Microwave, and Optical Technology Letters*, *International Journal of Microwave and Wireless Technologies*, *Scientific Reports*, *AEU International Journal of Communication and Electronics*, *Personal Wireless Communication*, and others. Prof. Abdalla served in the technical committee of many conferences in the areas of electromagnetic/electronic and communication. Prof. Abdalla was the recipient of the Egyptian encouragement state prize award for engineering sciences in 2014. In 2019, he was the recipient of the Egyptian El-sherouq innovation award in electronic engineering. He was awarded the top 1% Publon worldwide reviewer award for 2018 and 2019. In 2020, he was named in the top 2% of scientists in "A standardized citation metrics author database annotated for scientific field"/"Updated science-wide author databases of standardized citation indicators."

https://doi.org/10.1017/S1759078722001015 Published online by Cambridge University Press